Electronic supplementary information

Electrochemical Determination of Nitrofurantoin Using a Self-Templated NiFeCo Layered Double Oxide-Carbon Composite with Dynamic Fe Regeneration

Jiang-Tao Chen,[a] ‡ Ming-Dong Wang,[b] ‡ Fen-Ying Kong,[a] Tian-Pei Cai,[a] Lu-Mei Wang,[c] Juan-Juan Gao,*[a] and Wei Wang*[a]

[a] *School of Chemistry* and *Chemical Engineering, Yancheng Institute of Technology, Yancheng 224002, PR China*

[b] *School of Materials Science* and *Engineering, Yancheng Institute of Technology, Yancheng 224051, PR China*

[c] *School of Emergency Management* and *Safety Engineering, Yancheng Institute of Technology, Yancheng 224002, PR China*

‡ These authors contributed equally.

* Corresponding authors.

Tel/Fax: +86-515-88298186

E-mail address: gaojj@ycit.edu.cn (Juanjuan Gao)

wangw@ycit.edu.cn (Wei Wang)

1. Experimental

1.1 Chemicals and Materials

All chemicals were of analytical grade and used as received without further purification. Collagen-derived peptides (≈500 Da, 99%) were obtained from Xi'an Enpeptide Biotechnology Co., Ltd. Iron(III) nitrate nonahydrate ($Fe(NO_3)_3·9H_2O$), Nickel(II) nitrate hexahydrate ($Ni(NO_3)_2·6H_2O$), Cobalt(II) nitrate hexahydrate ($Co(NO_3)_2·6H_2O$), Urea (CH_4N_2O) were purchased from Aladdin Chemistry Co., Ltd. Nitrofurantoin (NFT), potassium ferricyanide ($K_3[Fe(CN)_6]$), potassium ferrocyanide trihydrate ($K_4[Fe(CN)_6]·3H_2O$), potassium chloride (KCl), Sodium phosphate monobasic monohydrate ($NaH_2PO_4·H_2O$), sodium hydrogen phosphate dihydrate ($Na_2HPO_4·2H_2O$), levofloxacin (LVFX), tetracycline (TC), and other inorganic salts and organic compounds were supplied by Shanghai Macklin Biochemical Technology Co., Ltd. Ultrapure water (18 MΩ cm) was prepared using a Milli-Q purification system (Millipore, USA).

1.2 Characterization

Fourier transform infrared (FT-IR) spectra were acquired on a Thermo Nicolet IS5 spectrometer over the scanning range of 4000–400 cm^{-1}. Thermogravimetric analysis (TGA) was performed on a TG/DAT7300 analyzer under a nitrogen atmosphere at a heating rate of 10°C min^{-1} from 25 to 800°C. Nitrogen adsorption-desorption isotherms were measured using a Micromeritics ASAP 2460 instrument to determine the specific surface area and pore structure of the samples, fafter degassing under vacuum at 150°C for 10 h. The crystalline phase and structure were analyzed by X-ray diffraction (XRD) using a D/max 2500 VL/PC diffractometer. The morphology and microstructure were observed by field-emission

transmission electron microscopy (FE-TEM, JEM-F200, 200 kV) and scanning electron microscopy (SEM, Sigma 300, Zeiss, Germany) equipped with an energy-dispersive X-ray spectroscopy (EDS, Oxford Xplore30) system. The elemental composition and valence states were analyzed by X-ray photoelectron spectroscopy (XPS, ESCALAB 250XI) using Al Kα radiation as the excitation source. Real samples were analyzed and validated by an Agilent 1200 high-performance liquid chromatography (HPLC).

1.3 Preparation of Layered Double Hydroxides (LDH)

NiFe layered double hydroxide (NiFe LDH) was synthesized via a urea-assisted hydrothermal method[1]. Briefly, 0.436 g (0.75 mmol) of $Ni(NO_3)_2 \cdot 6H_2O$, 0.202 g (0.25 mmol) of $Fe(NO_3)_3 \cdot 9H_2O$, and 0.720 g (6.00 mmol) of urea were dissolved in 60 mL of deionized water under magnetic stirring until a clear solution was obtained. The molar ratio of Ni to Fe was fixed at 3:1, while urea was added in a 6-fold molar excess relative to the total metal ions to facilitate homogeneous precipitation. The resulting solution was transferred into a 100 mL Teflon-lined stainless-steel autoclave and maintained at 120°C for 6 h. After naturally cooling to room temperature, the precipitate was collected by centrifugation, thoroughly washed with ultrapure water and ethanol, and then vacuum-dried at 60°C overnight to obtain NiFe LDH powder.

Under identical hydrothermal conditions, ternary NiFeCo layered double hydroxide (NiFeCo LDH) was synthesized by adjusting the metal precursor ratios. Specifically, 0.384 g (0.66 mmol) of $Ni(NO_3)_2 \cdot 6H_2O$, 0.178 g (0.22 mmol) of $Fe(NO_3)_3 \cdot 9H_2O$, 0.064 g (0.11 mmol) of $Co(NO_3)_2 \cdot 6H_2O$, and 0.720 g (6.00 mmol) of urea were dissolved in 60 mL of deionized water. The molar ratio of Ni:Fe:Co was set at 6:2:1, thereby maintaining the same

Ni:Fe ratio (3:1) as that of NiFe LDH to ensure comparable Fe active-site density. Subsequent hydrothermal treatment, product recovery, washing, and drying procedures were identical to those used for NiFe LDH synthesis.

1.4 Preparation of Layered Double Oxides Supported Carbon Composites

NiFeCo LDO-C composites were constructed via an integrated self-templating/self-etching strategy. Collagen peptides, a biopolymer primarily composed of collagen and rich in amino acids such as glycine, proline, and hydroxyproline, intrinsically contain abundant N and a small amount of S heteroatoms[2]. In a typical procedure, collagen-derived peptide precursor (0.5, 1.0, or 1.5 g) and 0.08 g of the as-synthesized NiFeCo LDH were co-dispersed in 30 mL of deionized water and magnetically stirred at room temperature for 2 h to ensure homogeneous mixing. The resulting suspension was subsequently frozen and freeze-dried for 24 h to obtain a porous composite precursor. The dried precursor was then thermally treated in a tubular furnace under a nitrogen atmosphere. The temperature was increased at a rate of 5°C min^{-1} to 600, 700, or 800 °C and maintained for 2 h to complete the pyrolysis and in situ composite formation. During this process, the LDH precursor was converted into layered double oxides (LDO), while the peptide was simultaneously transformed into a porous carbon framework. The resulting composites were denoted as NiFeCo LDO-$C_{x/y}$, where *x* represents the calcination temperature and *y* indicates the mass of the collagen peptides.

For comparison, several control samples were prepared under identical thermal conditions, including carbon derived from the collagen peptides without LDH (denoted as C), NiFe LDO-C composites obtained by replacing NiFeCo LDH with NiFe LDH, and pure LDO (NiFe LDO and NiFeCo LDO) obtained by direct calcination of the corresponding LDH

precursors without the carbon source.

1.5 Fabrication of the Electrochemical Sensor

Prior to modification, the glassy carbon electrode (GCE, 3 mm in diameter) was sequentially polished with 0.3 and 0.05 μm Al_2O_3 slurry until a mirror finish was achieved. It was then ultrasonically cleaned with ethanol and ultrapure water to remove any surface contaminants and ensure surface uniformity. To prepare the catalyst suspension, 5 mg of as-prepared NiFeCo LDO-C powder was dispersed in 2 mL of aqueous solution and sonicated for 1 hour to ensure uniform dispersion. Subsequently, 6 μL of the catalyst suspension was drop-cast onto the electrode surface and dried naturally at room temperature to form a uniform catalyst film, denoted as NiFeCo LDO-C/GCE. For comparison, control electrodes, including NiFe LDH/GCE, NiFeCo LDH/GCE, NiFeCo LDO/GCE, C/GCE, and NiFe LDO-C/GCE, were prepared using identical methods. Prior to measurement, the modified electrodes were activated by performing the continuous scans in phosphate-buffered solution (PBS, pH=7.0) until the stable voltammograms were obtained.

1.6 Electrochemical Measurements

All electrochemical experiments, including cyclic voltammetry (CV), differential pulse voltammetry (DPV), and electrochemical impedance spectroscopy (EIS), were performed using the CHI660E electrochemical workstation manufactured by Chenhua Instrument Co., Ltd. (Shanghai, China). A conventional three-electrode system was employed with platinum wire and a saturated Ag/AgCl reference electrode (3.0 M KCl electrolyte) as the auxiliary electrode and reference electrode, respectively, a bare GCE or modified electrode as working electrode.

1.7 Pretreatment of Real Samples

The actual samples include milk and honey purchased from supermarkets, as well as river water collected from urban rivers. The pretreatment procedures for milk and honey were performed as follows[3]: 4 mL of honey or 4 mL of milk was diluted to 10 mL with ultrapure water. Subsequently, 1 mL of chloroform and 1 mL of 10% (w/v) trichloroacetic acid was added, and then sonicated for 20 min to precipitate proteins and extract organic compounds. After sonication, the mixture was centrifuged at 10,000 rpm for 10 min to separate the precipitate. The obtained supernatant was filtered through a 0.22 μm membrane to remove lipids, neutralized with 0.05 M NaOH solution, and finally diluted 10-fold with ultrapure water for subsequent experiments. The river water sample was centrifuged to remove impurities and used directly without further pretreatment.

2. Formulas

Regarding the CV curve, certain parameters in the paper can be calculated using the following formulas:

(1) The electrochemical surface areas (ECSAs) can be determined by the Randles–Ševčík equation:

$I_{pc}=2.69\times10^{5}\times n^{3/2}\times A\times C\times D^{1/2}\times \upsilon^{1/2}$

Where I_{pc} represents the cathodic peak current (A), n is the number of electrons transferred, A refers to the effective surface area of the working electrode (cm^2), C indicates the concentration of the electroactive substrate (mol/cm^3), D is the diffusion coefficient of $Fe(CN)_6]^{3-/4-}$ (7.6×10^{-6} cm^2/s), υ denotes the scan rate (mV/s).

(2) The electron-transfer number (n) can be determined by the Laviron equation:

$$E_{pc}=E^{0}+(\frac{RT}{\alpha nF})\ln\left(\frac{RTK^{0}}{\alpha nF}\right)+\left(\frac{RT}{\alpha nF}\right)\ln\upsilon$$

$$\left|E_{pc/2}\text{-}E_{pc}\right|=1.857(\frac{RT}{\alpha F})$$

Where E^0 is the formal potential at temperature T, R is the ideal gas constant (8.314 J mol^{-1} k^{-1}), α is the charge-transfer coefficient, F is Faraday's constant (96,485 C mol^{-1}), K^0 is the standard heterogeneous rate constant, and $E_{pc/2}$ represents the half-peak potential.

3. Tables

Table S1 The component proportion and carbonization temperature of each group of samples

Samples	Collagen(g)	NiFe LDH (g)	NiFeCo LDH (g)	Temperature (°C)
NiFeCo LDO-$C_{0.5}$	0.5	—	0.08	700
NiFeCo LDO-$C_{1.0}$	1.0	—	0.08	700
NiFeCo LDO-$C_{1.5}$	1.5	—	0.08	700
NiFeCo LDO-$C_{600°C}$	1.0	—	0.08	600
NiFeCo LDO-$C_{700°C}$	1.0	—	0.08	700
NiFeCo LDO-$C_{800°C}$	1.0	—	0.08	800
NiFe LDO-C	1.0	0.08	—	700
C	1.0	—	—	700
NiFe LDO	—	0.08	—	700
NiFeCo LDO	—	—	0.08	700

Table S2 (a) Ni 2p and Fe 2p high-resolution XPS spectra deconvolution results of NiFe LDH, NiFeCo LDH, NiFeCo LDO, and NiFeCo LDO-C and NiFeCo LDO-C (after). (b) Co 2p high-resolution XPS spectra deconvolution results of NiFeCo LDH, NiFeCo LDO, and NiFeCo LDO-C and NiFeCo LDO-C (after).

(a)

Sample	Binding energy (eV)/relative%					
	Ni 2p		Fe 2p			
	$Ni^{2+}(2p_{1/2})$	$Ni^{2+}(2p_{3/2})$	$Fe^{3+}(2p_{1/2})$	$Fe^{2+}(2p_{1/2})$	$Fe^{3+}(2p_{3/2})$	$Fe^{2+}(2p_{3/2})$
NiFeCo LDO-C (after)	873.8/30.3	856/69.7	724.9/19.1	721.4/11.6	712.3/41.5	706.3/27.8
NiFeCo LDO-C	873.7/30	855.9/70	725.0/27.8	720.3/13.1	712.5/42.2	707.9/16.9
NiFeCo LDO	873.7/33.3	855.8/66.7	725.1/22.6	719.8/15.9	712.2/55.7	706.4/5.8
NiFeCo LDH	873.7/40.7	855.9/59.3	724.4/23.2	719.8/7.2	711.5/55.2	706.4/14.4
NiFe LDH	873.3/33.1	855.6/66.9	724.3/24.7	719.8/8.3	710.9/51.5	705.7/15.5

(b)

Sample	Binding energy (eV)/relative%			
	Co 2p			
	$Co^{2+}(2p_{1/2})$	$Co^{3+}(2p_{1/2})$	$Co^{2+}(2p_{3/2})$	$Co^{3+}(2p_{3/2})$
NiFeCo LDO-C (after)	798.8/16.3	796.5/23.8	784.8/15.8	781.7/44.1
NiFeCo LDO-C	798.4/20.3	796.7/19.3	783.5/27.0	780.7/33.4
NiFeCo LDO	797.9/7.4	796.2/9.7	783.4/26.1	780.4/56.8
NiFeCo LDH	797.4/5.3	795.8/11.1	783.3/25.1	780.3/58.5

Table S3 XPS peak parameters and relative contents of Fe 2p, Co 2p, and Ni 2p species of NiFeCo LDO-C before and after NFT reduction.

Species	Condition	Binding energy (eV)	relative%
Fe ($2p_{1/2}$)	Before	725.0 (Fe^{3+}), 720.3 (Fe^{2+})	Fe^{2+}: 30.0%, Fe^{3+}: 70.0%
Fe ($2p_{3/2}$)		712.5 (Fe^{3+}), 707.9 (Fe^{2+})	
Fe ($2p_{1/2}$)	After	724.9 (Fe^{3+}), 721.4 (Fe^{2+})	Fe^{2+}: 39.4%, Fe^{3+}: 60.6%
Fe ($2p_{3/2}$)		712.3 (Fe^{3+}), 706.3 (Fe^{2+})	
Co ($2p_{1/2}$)	Before	798.4 (Co^{2+}), 796.7 (Co^{3+})	Co^{2+}: 47.3%, Co^{3+}: 52.7%
Co ($2p_{3/2}$)		783.5 (Co^{2+}), 780.7 (Co^{3+})	
Co ($2p_{1/2}$)	After	798.8 (Co^{2+}), 796.5 (Co^{3+})	Co^{2+}: 31.1%, Co^{3+}: 67.9%
Co ($2p_{3/2}$)		784.8 (Co^{2+}), 781.7 (Co^{3+})	
Ni ($2p_{1/2}$)	Before	873.7 (Ni^{2+})	Ni^{2+}: 100%
Ni ($2p_{3/2}$)		855.9 (Ni^{2+})	
Ni ($2p_{1/2}$)	After	873.8 (Ni^{2+})	Ni^{2+}: 100%
Ni ($2p_{3/2}$)		856 (Ni^{2+})	

Table S4 The R_{ct} values of all samples obtained from the semicircle diameter of EIS at higher frequency

Samples	R_{ct} (Ω)	Electrolyte
NiFeCo LDO-C/GCE	228.7	
C/GCE	930.2	
NiFeCo LDO/GCE	650.8	
NiFe LDO/GCE	747.5	$[Fe(CN)_6]^{3-/4-}$
NiFeCo LDH/GCE	1269.0	
NiFe LDH/GCE	1310.4	
Bare GCE	1351.5	

Table S5 The I_{pc}, ΔE_p and ECSAs for Bare GCE, C/GCE, NiFeCo LDO/GCE and NiFeCo LDO-C/GCE

Electrodes	I_{pc} (μA)	ΔE_p (V)	ECSAs $\times 10^{-2}$ (cm^2)
NiFeCo LDO-C/GCE	114.1	0.11	7.52
NiFeCo LDO/GCE	92.75	0.15	5.97
C/GCE	88.77	0.28	5.38
Bare GCE	78.32	0.26	4.90

Table S6 Recovery results of NFT spiked in different samples.

Sample	Spiked (μM)	Found[a] (μM)		Recovery ± RSD (%, *n* = 3)	
		DPV	HPLC	DPV	HPLC
Honey	0	–	–	–	–
	25.00	25.18	26.05	100.64±2.04	106.70±0.31
	50.00	49.19	51.26	98.47±0.90	102.52±4.29
	75.00	76.16	76.47	100.80±1.67	101.96±1.88
Milk	0	–	–	–	–
	25.00	25.03	26.58	100.12±0.34	104.23±1.65
	50.00	50.13	46.59	100.24±1.43	93.18±0.20
	75.00	74.56	70.90	99.82±1.02	94.53±1.70
River water	0	–	–	–	–
	25.00	25.44	25.21	101.57±1.35	100.82±2.01
	50.00	49.58	52.30	99.21±0.96	104.59±2.91
	75.00	75.70	75.11	100.51±1.33	100.15±1.11

[a] Average of three measurements.

4. Figures

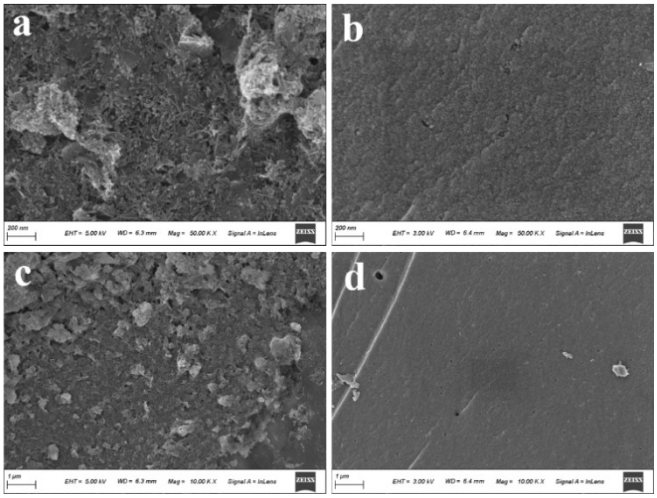

Fig. S1. SEM images of NiFeCo LDH (a, c) and C (b, d) with different magnification.

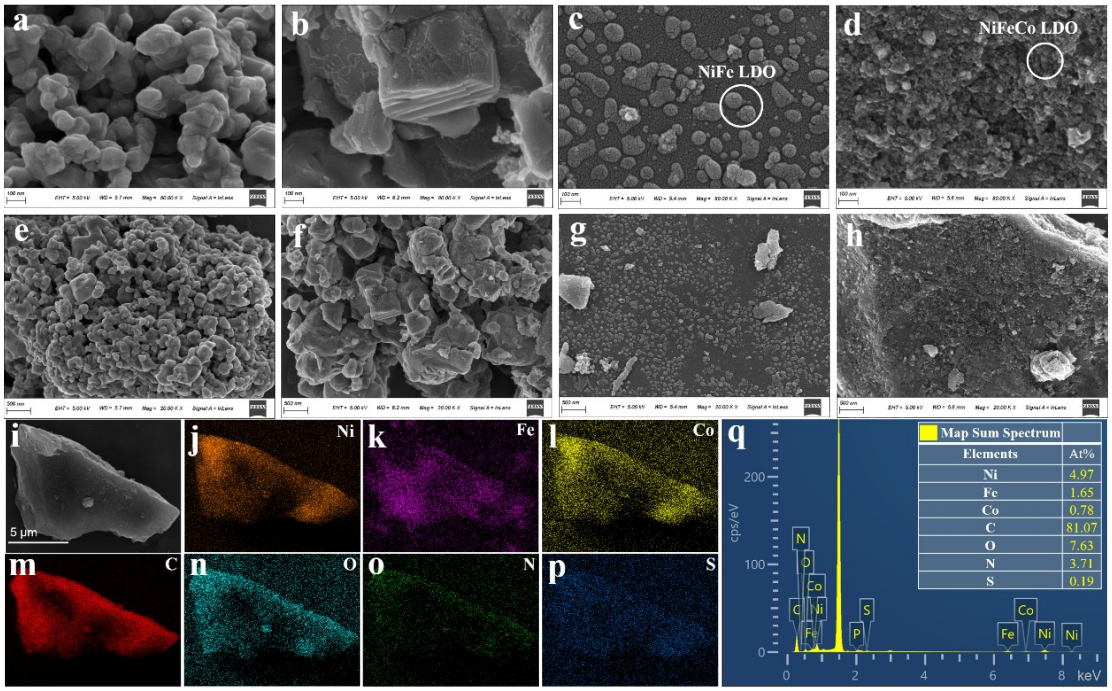

Fig. S2. SEM images of (a, e) NiFe LDO, (b, f) NiFeCo LDO, (c, g) NiFe LDO-C and (d, h) NiFeCo LDO-C with different magnification. (i–p) EDS elemental mapping and (q) elemental composition of NiFeCo LDO-C.

The morphological features of the NiFeCo LDH precursor, C, and their derived materials (NiFe LDO, NiFeCo LDO, NiFe LDO-C, and NiFeCo LDO-C) are shown in Fig. S1 and Fig. S2. The NiFeCo LDH precursor exhibits a typical lamellar morphology with well-defined flake-like nanosheets (Fig. S1a, c). After calcination, NiFeCo LDH transforms into NiFeCo

LDO, accompanied by structural relaxation and the formation of a more open and porous architecture (Fig. S2b, f) [4]. This structural evolution effectively increases the number of accessible active sites and facilitates mass transport during electrochemical reactions. Compared with NiFe LDO (Fig. S2a, e), the introduction of Co results in more uniform nanosheets with clearer edges, indicating improved structural stability and regulated crystal growth [5]. SEM images of NiFeCo LDO-C (Fig. S2d, h) show that the nanosheets are interconnected and partially coated by the carbon matrix, while maintaining the inherited layered framework. The composite exhibits increased surface roughness and abundant pores, which are attributed to gas-assisted etching during concurrent pyrolysis. In contrast, the C without template support undergoes pyrolysis and presents a bulk amorphous morphology (Fig. S1b, d), and NiFe LDO-C shows partial structural collapse, suggesting that Co incorporation plays a key role in maintaining structural integrity during carbonization [6]. As a result, the overall morphological framework is preserved during severe dehydration and phase transformation, thereby providing a rigid self-template essential for uniform carbon coating and effective self-etching pore construction.

SEM–EDS analysis was performed to evaluate the elemental composition and distribution of NiFeCo LDO-C (Fig. S2i–q). Elemental mapping confirms the uniform distribution of Ni, Fe, and Co within the carbon matrix. The atomic ratio of Ni:Fe:Co (~6:2:1) is consistent with the designed precursor compositions. In addition, O, N, and S are uniformly present in the carbon matrix, indicating successful heteroatom doping derived from collagen. These provide abundant anchoring sites for metal species and promote charge transfer during electrochemical sensing.

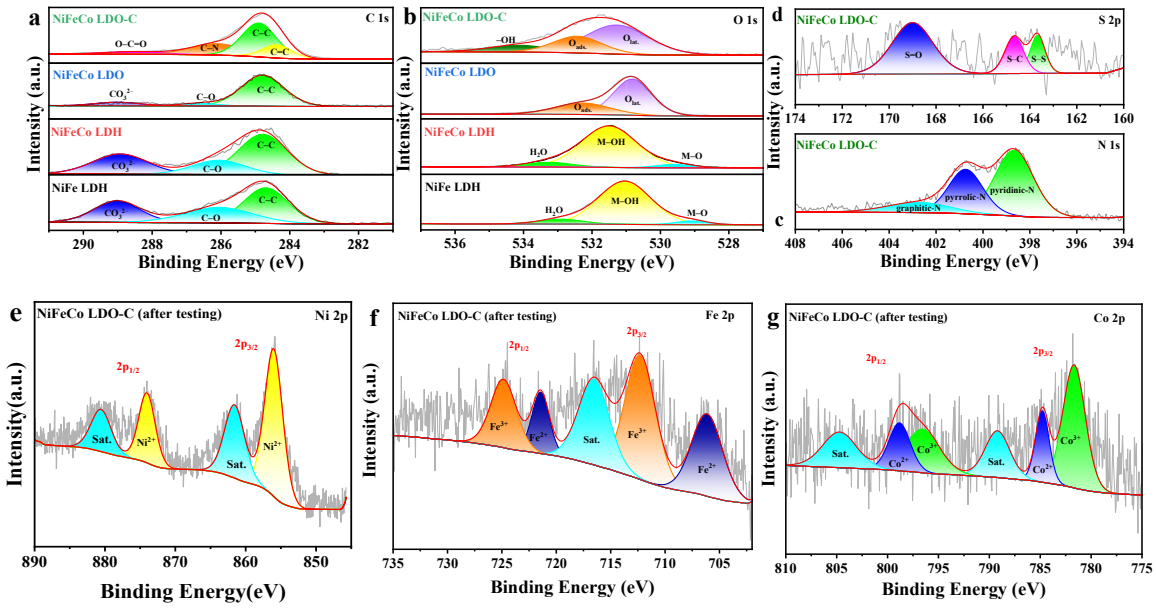

Fig. S3. High-resolution XPS spectra of (a) C 1s, and (b) O 1s for NiFe LDH, NiFeCo LDH, NiFeCo LDO, and NiFeCo LDO-C. (c) N 1s and (d) S 2p spectra of NiFeCo LDO-C. High-resolution XPS spectra of (e) Ni 2p, (f) Fe 2p, (g) Co 2p, for NiFeCo LDO-C (after testing).

The C 1s spectrum of NiFeCo LDO-C (Fig. S3a) resolves into O–C=O, C–N, C–C (sp^3), and C=C (sp^2) components [2, 7, 8]. In contrast, LDH exhibits peaks at 289.0 and 286.2 eV, assigned to interlayer CO_3^{2-} and C–O in hydrotalcite [7], consistent with FT-IR and XRD results confirming CO_3^{2-} as the dominant interlayer anion. The weak C–C signal originates from adventitious carbon during XPS measurement.

The O 1s spectrum of NiFeCo LDO-C (Fig. S3b) consists –OH, adsorption oxygen ($O_{ads.}$) and lattice oxygen ($O_{lat.}$) [4, 9]. The–OH peak is absent in NiFeCo LDO, likely due to its lower hydrophilicity. While the O1s spectra of NiFe LDH and NiFeCo LDH mainly contains H_2O, M–OH and M–O peaks [7, 10]. The N 1s spectrum (Fig. S3c) reveals pyridinic-N, pyrrolic-N and graphitic-N species, which introduce defects, regulate local electron density, and enhance conductivity [2]. The S 2p spectrum (Fig. S3d) exhibits characteristic peaks at 169.0, 164.6, and 163.6 eV, assigned to S=O, S–C and S–S bonding states, respectively. The incorporation

of S not only increases the density of electrochemically active sites but also expands the carbon layers, potentially facilitating rapid NFT insertion/extraction. Overall, the co-doping of N and S introduces abundant defects and synergistically tunes the local electronic structure of the carbon matrix, thereby increasing active site density, enhancing electrical conductivity, and accelerating ion diffusion. These combined effects underpin the superior electrochemical kinetics and long-term stability of the NiFeCo LDO-C composite [9].

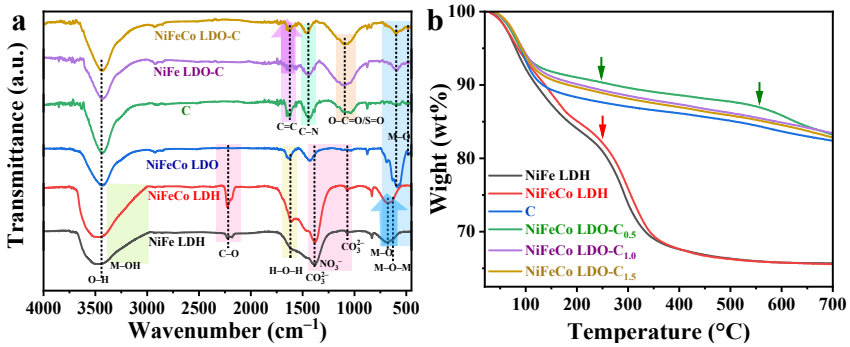

Fig. S4. (a) FT-IR spectras of NiFe LDH, NiFeCo LDH, NiFeCo LDO. (b) TGA curves of NiFe LDH, NiFeCo LDH and NiFeCo LDO-C_y (y = 0.5 g, 1.0 g and 1.5 g).

The molecular structures of the as-prepared samples were further investigated by FT-IR spectroscopy (Fig. S4a). Both NiFe LDH and NiFeCo LDH display characteristic features of LDH frameworks. The broad band at ~3440 cm^{-1} and the shoulder at ~1615 cm^{-1} correspond to O–H stretching and H–O–H bending vibrations of interlayer water, respectively [5, 11, 12]. The band in 3000–3400 cm^{-1} region is assigned to hydrogen-bonded M–OH groups within the hydroxide layers [13]. The absorptions at ~1360 and ~900 cm^{-1} are attributed to the asymmetric stretching and bending vibrations of CO_3^{2-}, confirming their role as the primary charge-balancing interlayer anion [13, 14]. The feature at ~2220 cm^{-1} further supports the presence of carbonate species. The pronounced broadening of the ~1360 cm^{-1} band, together with weak absorption near ~1000 cm^{-1}, suggests minor residual NO_3^- originating from metal

salt precursors [14]. The bands at ~665 and ~630 cm^{-1} are associated with M–O stretching and the M–O–M lattice vibrations [5, 15, 16]. Compared with NiFe LDH, NiFeCo LDH exhibits stronger M–O vibration intensity, implying structural modulation induced by Co incorporation, consistent with the XRD results.

Upon calcination, the LDH precursor reconstructs into LDO with the removal of interlayer species. The sharp CO_3^{2-} (~1360 cm^{-1}) and H_2O (~1600 cm^{-1}) bands are markedly weakened, and the C–O vibration at ~2220 cm^{-1} disappears, confirming the decomposition of interlayer carbonate and water, although a small residual fraction remains. The broad O–H band near ~3430 cm^{-1} remains but is mainly attributed to surface-adsorbed moisture. Meanwhile, new broad absorptions at ~570 and ~450 cm^{-1} appear, corresponding to M–O vibrations of the reconstructed oxide phase, consistent with the XRD results.

For C material, the band at ~1600 cm^{-1} corresponds to the stretching vibration of aromatic sp^2-hybridized C=C bonds [17]. The peak at ~1430 cm^{-1} is assigned to C–N stretching [9]. while the broad band near ~1100 cm^{-1} is indexed to O–C=O or S=O vibrations [14]. These features indicate the presence of heteroatom-containing functional groups on the carbon surface. Compared with NiFeCo LDO, the NiFeCo LDO-C composite exhibits a pronounced absorption near ~1600 cm^{-1}, corresponding to the C=C stretching vibration of the carbon matrix, confirming successful carbon incorporation. The absence of the CO_3^{2-} (~1360 cm^{-1}) indicates complete decomposition of carbonate species after calcination. The broad absorptions in the 400–700 cm^{-1} region are characteristic of M–O vibrations of the oxide phase, with peak broadening arising from nanoscale crystallite effects and carbon encapsulation. In NiFe LDO-C, the characteristic C=C stretching band near ~1600 cm^{-1} is

barely discernible. In the absence of Co-induced structural stabilization, NiFe LDH undergoes partial structural collapse during carbonization, leading to a composite that more closely resembles a physical mixture of metal oxides and carbon. As a result, the carbon phase fails to form a continuous and well-integrated conductive network, giving rise to a weak infrared response. In contrast, the pronounced carbon-related absorption observed in NiFeCo LDO-C indicates the formation of a homogeneous nanoscale metal oxide–carbon composite via a self-templated carbonization process.

The thermal decomposition behaviors of NiFe LDH and NiFeCo LDH were analyzed by TGA (Fig. S4b). Both samples exhibit two main weight-loss stages. The initial mass loss below 200°C corresponds to the removal of adsorbed and interlayer water, while the second loss between 250 and 350°C originates from the decomposition of interlayer CO_3^{2-} and the dehydroxylation of metal hydroxide layers, leading to oxide formation [13]. Above 500°C, the mass loss becomes negligible, and the total weight loss at 700°C reaches approximately 34%, consistent with the removal of water and CO_3^{2-} observed in FT-IR. In contrast, all NiFeCo LDO-C_y composites display higher residual mass ratios (~83%) than pristine LDH (~70%), indicating the successful incorporation of thermally stable carbon. The slightly reduced overall weight loss relative to pure carbon suggests enhanced thermal stability due to metal–carbon interaction. Among the composites, NiFeCo LDO-$C_{0.5}$ exhibits a distinct transition near ~250°C owing to its lower carbon content. The weight loss below 120°C is mainly associated with water desorption, while the subsequent loss between 150 and 350°C arises from the overlap of LDH decomposition and the initial pyrolysis of unstable carbon functional groups. With increasing carbon loading, the thermal behavior becomes

increasingly dominated by carbon pyrolysis. At higher temperatures (>550°C), the accelerated weight loss is attributed to further aromatization and structural ordering of the carbon skeleton, possibly accompanied by the release of small gaseous species. This process is likely facilitated by the catalytic effect of LDO. Importantly, the decomposition temperature range of LDH in the composites remains comparable to that of pristine LDH, indicating that carbon introduction does not alter the intrinsic thermal transformation pathway.

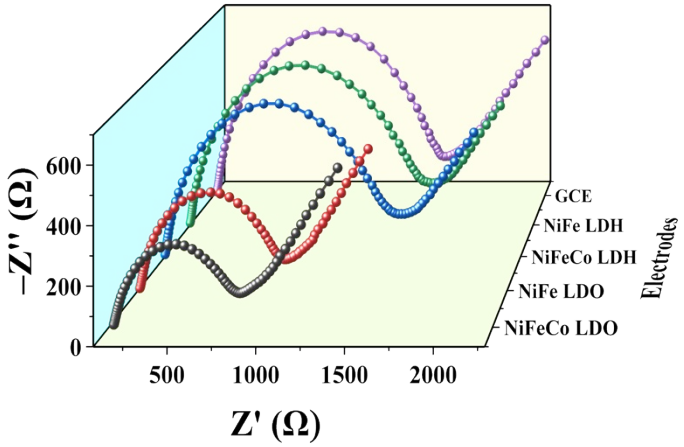

Fig. S5. EIS characterization of bare GCE, NiFe LDH/GCE , NiFeCo LDH/GCE, NiFe LDO/GCE and NiFeCo LDO/GCE in 0.1 M KCl solution containing 5 mM $[Fe(CN)_6]^{3-/4-}$.

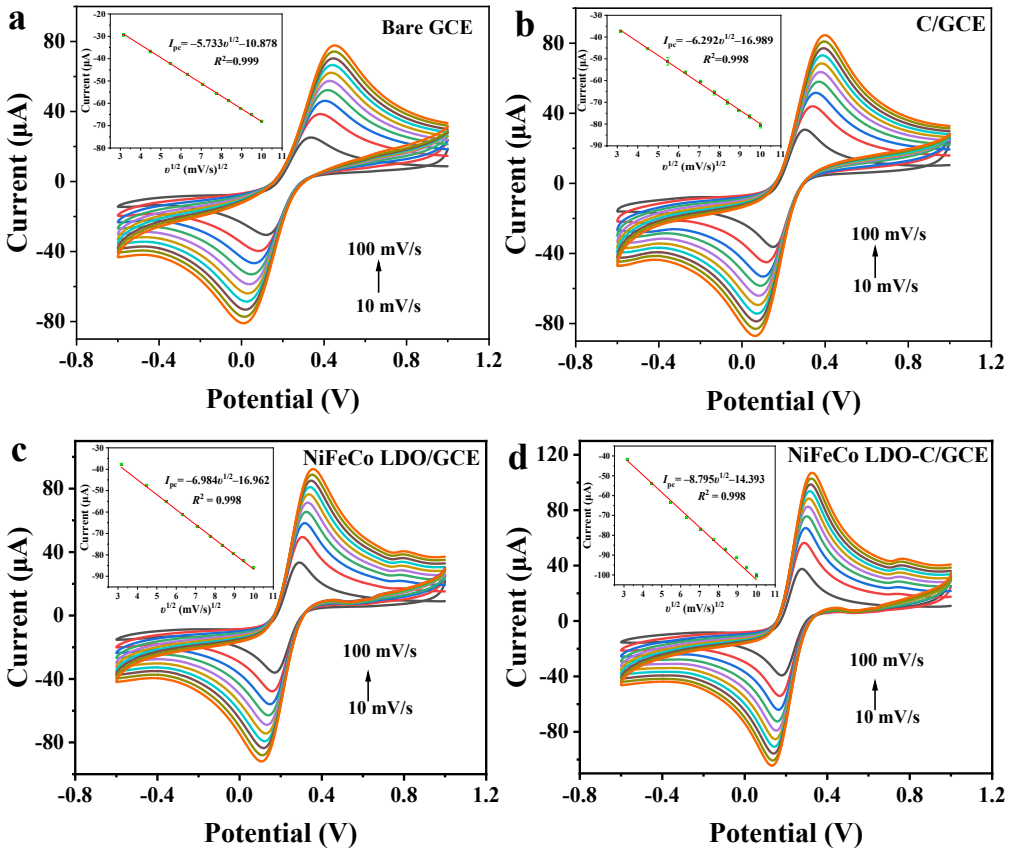

Fig. S6. CVs profiles of different electrodes at scan speeds from 10 to 100 mV/s in 5.0 mM $[Fe(CN)_6]^{3-/4-}$ solution with 0.1 M KCl: (a) Bare GCE, (b) C/GCE, (c) NiFeCo LDO/GCE and (d) NiFeCo LDO-C/GCE. The upper left insets: square root of scan rate vs. current response.

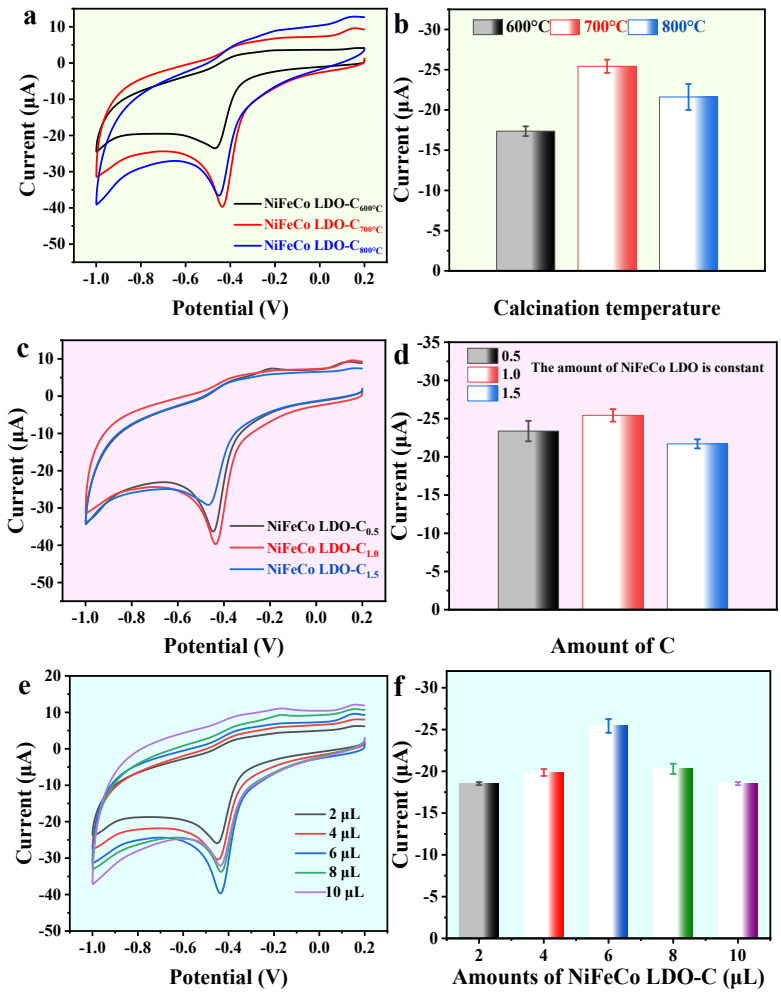

Fig. S7. (a) The impact of calcination temperature on NiFeCo LDO-C/GCE in the 0.1 M PBS solutions (pH = 7.0) containing 200 μM NFT, (b) The bar diagram of (a). (c) The impact of the amount of C on NiFeCo LDO-C/GCE, (d) The bar diagram of (c). (e) The impact of the drop-coating amount of NiFeCo LDO-C/GCE, (f) The bar diagram of (e).

To evaluate the effect of calcination temperature, NiFeCo LDO-C samples prepared at different temperatures were compared. As shown in Fig. S7a,b, the catalyst calcined at 700°C exhibits the highest current response. The inferior performance at 600°C is attributed to incomplete decomposition and limited conductivity, whereas 800°C likely induces particle sintering and loss of heteroatom functionalities. Therefore, 700°C was selected as the optimal calcination temperature.

The influence of the C/NiFeCo ratio was evaluated by varying the carbon content (Fig. S7c,d). NiFeCo LDO-$C_{1.0}$/GCE exhibits the highest current response. Lower carbon content (0.5) results in limited conductivity, whereas excessive carbon (1.5) may shield active sites and disturb the metal valence balance due to over-reduction. Thus, NiFeCo LDO-$C_{1.0}$ was selected for subsequent experiments. The catalyst loading on GCE was further optimized (Fig. S7e,f). The peak current increases with loading volume and reaches a maximum at 6 µL. Higher loadings decrease the response due to mass-transfer limitations, while lower loadings provide insufficient coverage [18]. Therefore, 6 µL was used in the following measurements.

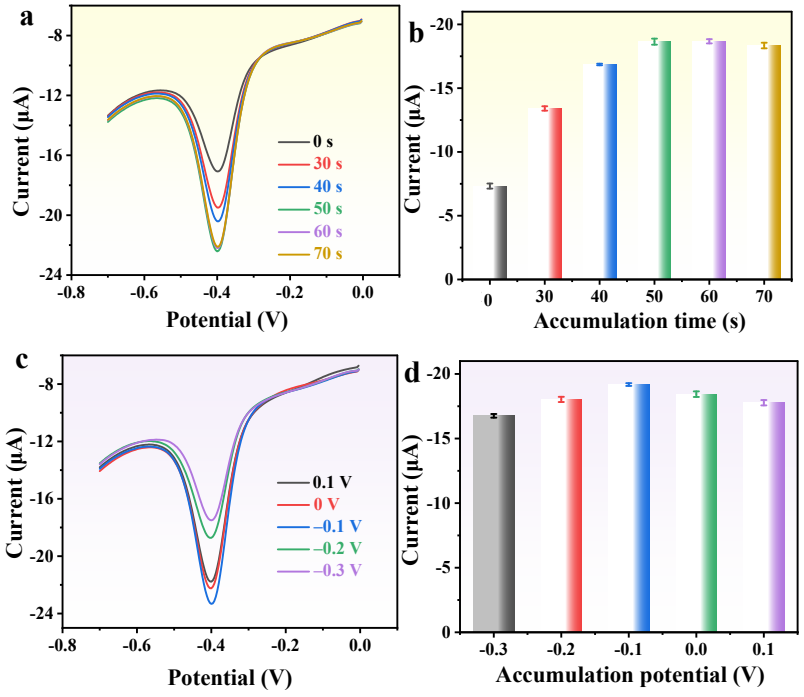

Fig. S8. (a) CV curves of NiFeCo LDO-C/GCE at different accumulation times (Time = 0 s, 30 s, 40 s, 50 s, 60 s, 70 s) with 100 µM addition of NFT and (b) the bar diagram of the peak current response of NFT with different accumulation time. (c) CV curves of the peak current response of 100 µm NFT measured at different potentials of using NiFeCo LDO-C/GCE and (d) the bar diagram of the peak current response of NFT with different accumulation potentials.

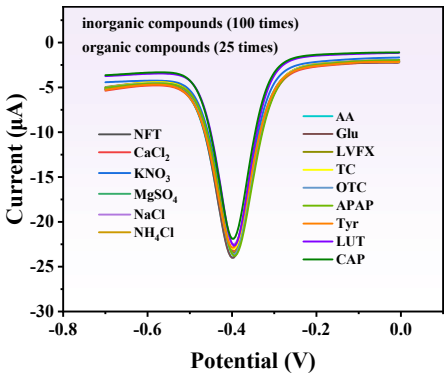

Fig. S9. DPV of selectivity study in the presence of NFT and addition of various interfering species.

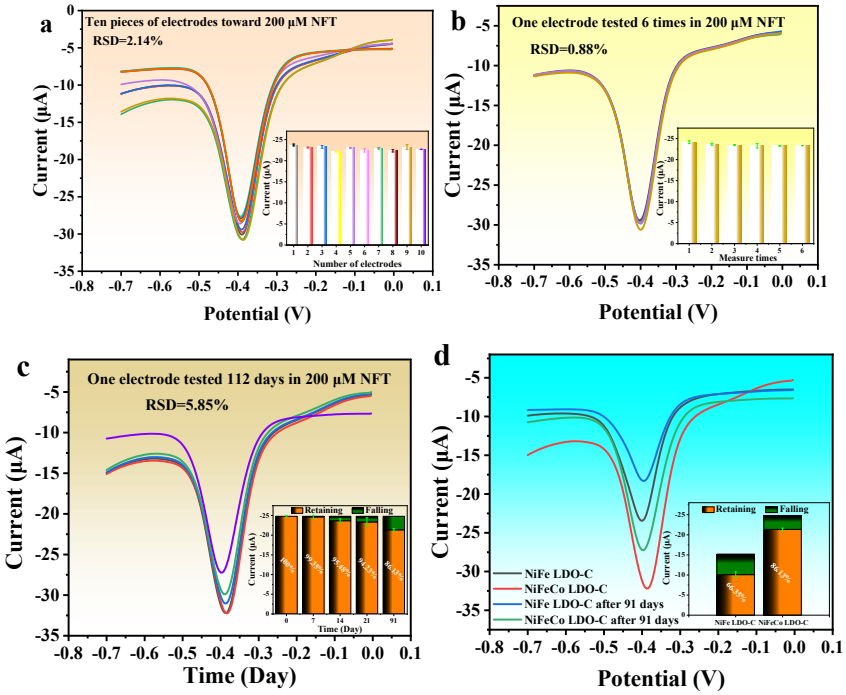

Fig. S10. (a) Reproducibility for ten NiFeCo LDO-C/GCE. (b) Repeatability of the electrode. (c) The stability of the electrode. (d) Comparison of the stability of NiFe LDO-C/GCE and NiFeCo LDO-C/GCE.

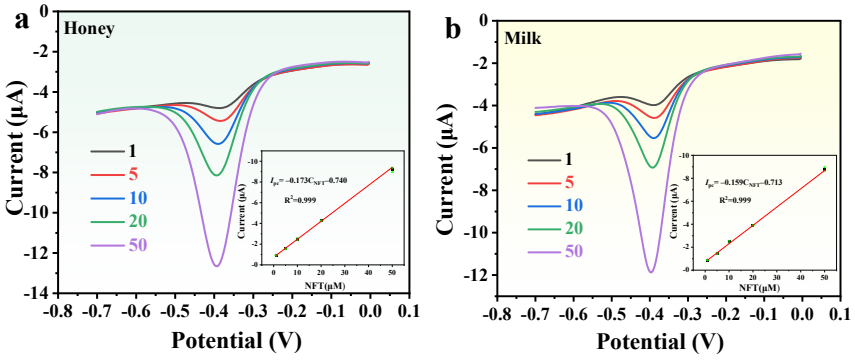

Fig. S11. DPV responses for (a) honey and (b) milk samples spiked with different amounts of NFT.

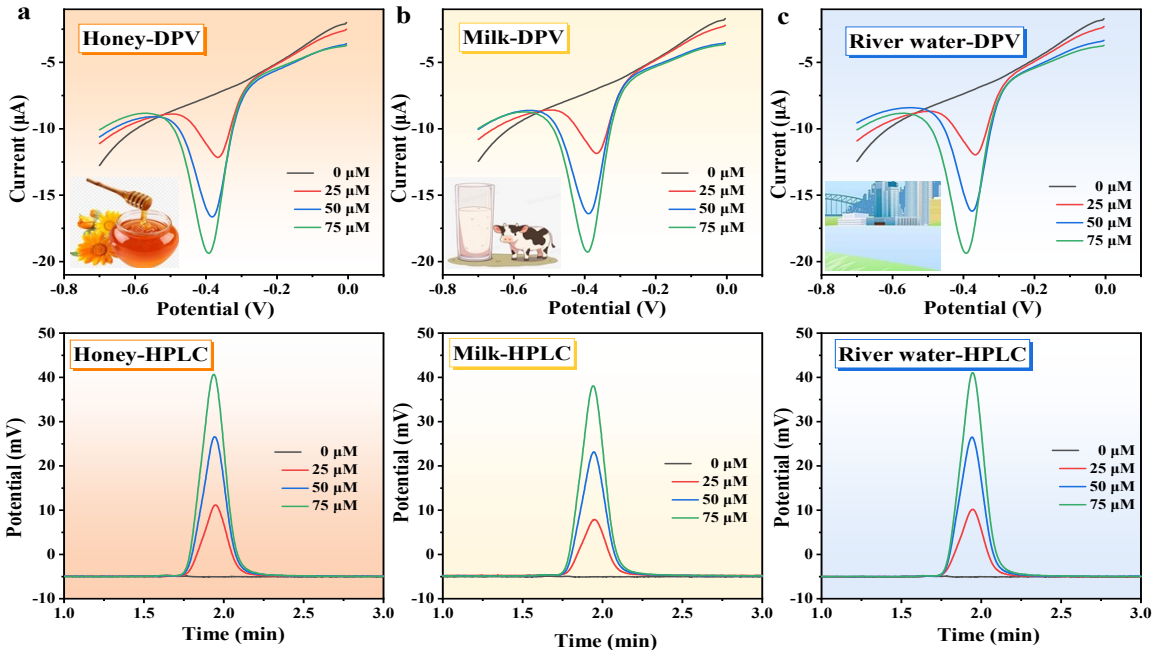

Fig. S12. (a-c) DPV and HPLC responses for honey, milk and river water samples spiked with different amounts of NFT

References

1. S. Assavachin, S. Ittisanronnachai, T. Atithep, N. Chitterisin and M. Sawangphruk, *J. Power Sources*, 2025, **650**.
2. M. Guo, H. Zhang, L. Luo, Z. Huang, D. Zhang, C. Gao, F. Gao, X. Chen, M. Terrones and Y. Wang, Carbon, 2024, **217**, 118631.
3. M. Liu, T. Zhe, F. Li, L. Zhu, S. Ouyang and L. Wang, *Food Chem.*, 2024, **461**, 140915.
4. Y. Shen, M. J. Martín de Vidales, G. Gorni, A. Gómez-Herrero, F. Fernández-Martínez and A. J. Dos santos-García, *Chem. Eng. J.*, 2022, **444**, 136610.
5. Y. Lin, H. Wang, C.-K. Peng, L. Bu, C.-L. Chiang, K. Tian, Y. Zhao, J. Zhao, Y.-G. Lin, J.-M. Lee and L. Gao, Small, 2020, **16**, 2002426.
6. P. Guo, D. Liu, H. Yang, P. Chen, M. Zhang, X. Ding, C. Zheng, H. Pan and R. Wu, *ACS Nano*, 2026.
7. H. Li, C. Wang, J. Qiu, H. Song, Q. Lai, T. Zhou, C. Han, J. Li, S. Yang, H. He, A. Li, B. Li, Y. Liang and S. Zhang, *J. Environ. Chem. Eng.*, 2025, **13**, 119731.
8. M. Ayiania, M. Smith, A. J. R. Hensley, L. Scudiero, J.-S. McEwen and M. Garcia-Perez, Carbon, 2020, **162**, 528-544.
9. Q. Zhou, R. Chen, Y. Chen, Y. Sun, J. Yuan, J. Xu, X. Liao, B. Shi and X. Xiao, *Ind. Crops Prod.*, 2025, **229**, 120977.
10. J. Hu, X. Xiong, W. Guan, Y. Chen and H. Long, *Sens. Actuators, B*, 2024, **401**, 135082.
11. H. Chen, Y. Ma, Y. Han, X. Mao, Y. Hu, X. Zhao, Q. Dong, B. Wen, A. Du, X. Wang, X. Lyu and Y. Jia, Small, 2024, **20**, 2309689.
12. X. Meng, Y. Wang, X. Song, M. Zhang, J. Yu, L. Qiu, J. Lin and X. Wang, ACS Appl. Mater. Interfaces, 2023, **15**, 48818-48825.
13. S. Assavachin, S. Ittisanronnachai, T. Atithep, N. Chitterisin and M. Sawangphruk, J. Power Sources,

2025, **650**, 237494.
14. C. Qiao, Z. Usman, T. Cao, S. Rafai, Z. Wang, Y. Zhu, C. Cao and J. Zhang, Chem. Eng. J., 2021, **426**, 130873.
15. P. Chen, X. Duan, G. Li, X. Qiu, S. Wang, Y. Huang, A. Stavitskaya and H. Jiang, Int. J. Hydrog. Energy, 2023, **48**, 7170-7180.
16. Y. Li, M. Lu, Y. Wu, H. Xu, J. Gao and J. Yao, Adv. Mater. Interfaces, 2019, **6**, 1900290.
17. Y. Zhu, W. Zhao, J. Zhang, Z. An, X. Ma, Z. Zhang, Y. Jiang, L. Zheng, X. Shu, H. Song, X. Xiang and J. He, ACS Catal., 2020, **10**, 8032-8041.
18. C. Zu, X. Peng, Y. Long, M. Peng, C. Wang, H. Zhang, Z. Tan, Y. He and Z. Bai, J. Alloys Compd., 2025, **1042**, 184173.